# Robust Causality Characterization via Generalized Dispersion Relations

Piero Triverio, *Student Member, IEEE*, and Stefano Grivet-Talocia, *Senior Member, IEEE*

*Abstract*—The self-consistency of frequency responses obtained via numerical simulations or measurements is of paramount importance in the analysis and design of linear systems. In particular, tabulated responses with flaws and causality violations have been demonstrated to be the root cause for numerical problems and unreliability in modeling and simulation tasks. In this work, we present the generalized dispersion relations as a robust and reliable tool for the causality characterization of frequency responses. Several applications are presented, including causality and passivity verification for tabulated data and causality-controlled interpolation schemes. Practical examples illustrate the excellent performance of the proposed techniques.

*Index Terms*—Causality, dispersion relations, Hilbert transform, interpolation, passivity.

## I. INTRODUCTION

**E**LECTRICAL interconnects play a key role in the performance of high-speed digital systems. They must route over long complex paths hundreds of digital signals, switching at clock frequencies often in the gigahertz range. Therefore, a proper interconnect design is crucial for the overall system performance, in order to avoid signal integrity problems. A successful design can only be carried out with accurate and reliable modeling and simulation tools in a computer-aided design (CAD) environment.

A standard approach for interconnect simulation is macromodeling. Interconnects are commonly represented in standard circuit simulators via black-box models obtained from input-output frequency responses. The latter are available either from direct measurements or from numerical field simulations. In order to obtain well-posed models, the raw frequency data must be physically consistent, i.e., coherent with the fundamental properties of the original structure: causality, stability and passivity. Unfortunately, the consistency of measured frequency responses may be compromised by several factors like measurement errors, wrong calibration procedures, and human mistakes. Similarly, convergence errors, wrong settings, or unphysical assumptions may lead to flawed results even when using state of the art electromagnetic solvers. Since inconsistent data are one of the main causes for CAD tools failure, robust methods to analyze and possibly improve the quality of raw frequency data are highly desirable.

In this paper, we propose several algorithms for data qualification based on a robust implementation of a special form of dispersion relations. Dispersion relations are the counterpart of the causality principle in the frequency domain. They consist of a pair of integral relations strongly linking the real and imaginary parts of any physical frequency response. Discovered by Kramers [1] and Krönig [2], the dispersion relations can be exploited for several purposes and, due to their global validity, they have been used in almost all areas of physics, science, and engineering. A brief history and a comprehensive set of bibliographic references on dispersion relations can be found in [3]. In electronics, dispersion relations have been used for measured data reconstruction [4], correction [5], extrapolation [6], time-domain inversion [7], and delay extraction [8].

A frequency response is causal when invariant upon application of the dispersion relations, i.e., when it can be reconstructed with no error from the dispersion relation operator. This suggests a simplistic approach for causality check: apply the dispersion relations and take the difference between the result and the original data. If this difference is smaller than a prescribed threshold, the original response is causal, otherwise it is not causal. Such test is obviously ill-defined, since highly dependent on the choice of the threshold. Moreover, application of dispersion relations to practical data, typically known over a limited bandwidth and at discrete frequencies only, is a very critical task [9], [3], [10]–[12]. The approximation errors due to the finite set of available samples may be so large to compromise the resolution of the causality test.

Two conditions must hold for insuring a sound numerical causality test. First, the numerical error in the evaluation of the dispersion relations must be small. Second, a good estimate or a bound for this error must be available, in order to quantify the numerical resolution of the test. Causality violations will be detectable only when larger than this numerical resolution.

This paper presents for the first time a numerical scheme that fulfills both conditions, hence guarantees a sound causality test for practical data. First, the minimization of the numerical error is achieved by employing the so-called *generalized dispersion relations*, also known as *dispersion relations with subtractions* or *generalized Hilbert transform*, which are intrinsically less sensitive to missing frequency points in the data (e.g., the high-frequency portion of a bandlimited response). We present an accurate scheme for their numerical evaluation, based on singularity extraction. Second, we provide rigorous and tight bounds for the unavoidable numerical errors due to both bandwidth truncation and discretization. The combination of these features allows the definition of a numerically robust causality test. The excellent performance of the proposed technique is illustrated by considering several possible applications. We re-

mark that, although the applications presented in this work are focused on electrical interconnects, the scope of this study is quite general, since the main results are applicable to any field of physics and science where linear and time-invariant systems are encountered.

This paper is organized as follows. Section II presents some background material on causality and dispersion relations. Also, the notation that will be used throughout this work is introduced. In Section III, the generalized dispersion relations are presented, together with a detailed analysis of all sources of errors involved in their numerical evaluation. This section includes a detailed comparison of proposed approach with existing techniques, showing how the state of the art is improved. In Section IV, a robust and accurate causality check scheme based on generalized dispersion relations is presented. In Section V, the technique is applied to verify the passivity of tabulated scattering responses. Finally, in Section VI, a causality-constrained interpolation scheme is presented.

## II. CAUSALITY AND DISPERSION RELATIONS

In this section, we recall some fundamental properties of linear systems with particular emphasis on the causality principle, from which dispersion relations derive.

### A. Linear Systems and Causality

We consider linear and time-invariant (LTI) electrical $p$-port networks, with input and output identified by the $p$-elements vectors $\mathbf{x}(t)$ and $\mathbf{w}(t)$, respectively. This description includes common network representations, e.g., impedance ($\mathbf{x}$ being currents and $\mathbf{w}$ voltages), admittance ($\mathbf{x}$ being voltages and $\mathbf{w}$ currents), and scattering (both $\mathbf{x}$, $\mathbf{w}$ being power waves). In the LTI case, the response $\mathbf{w}(t)$ can be written as the convolution between the input $\mathbf{x}(t)$ and the impulse response $\mathbf{h}(t)$ [13]

$$\mathbf{w}(t) = \mathbf{h}(t) * \mathbf{x}(t) = \int_{-\infty}^{+\infty} \mathbf{h}(t-\tau)\mathbf{x}(\tau)d\tau. \quad (1)$$

For a network with $p$ ports, $\mathbf{h}(t)$ is a $p \times p$ matrix of scalar functions $h_{ij}(t)$, each one representing the response observed at port $i$ when an ideal impulse (a Dirac's delta) is applied at port $j$, with all other inputs vanishing. The matrix $\mathbf{h}(t)$ describes completely the system behavior and includes important information about its fundamental physical properties. Causality, which is one of these properties, is the main subject of this work.

The causality principle states that no effect can precede in time its cause. The mathematical condition that identifies a LTI causal system is defined by the following theorem [13].

*Theorem 1:* A LTI system is causal if and only if all the elements $h_{ij}(t)$ of its impulse response matrix $\mathbf{h}(t)$ are vanishing for $t < 0$, i.e.,

$$\mathbf{h}(t) = 0, \quad t < 0. \quad (2)$$

### B. Dispersion Relations

Dispersion relations are the frequency-domain counterpart of (2), and any causal frequency response, defined as the standard Fourier transform of the impulse response

$$\mathbf{H}(j\omega) = \mathfrak{F}\{\mathbf{h}(t)\} = \int_{-\infty}^{+\infty} \mathbf{h}(t)e^{-j\omega t}dt, \quad (3)$$

must comply with them. They are of paramount importance, since LTI systems are naturally described, analyzed and designed in frequency domain. We provide in the following paragraph a brief derivation of dispersion relations, in order to present the necessary background material for the new developments of Section III.

For simplicity, we consider a scalar impulse response $h(t)$, although the whole derivation holds also in the multidimensional case for any element of the matrix $\mathbf{h}(t)$. Because of (2), any causal impulse response satisfies

$$h(t) = \text{sign}(t)h(t),$$

where $\text{sign}(t)$ is the sign function that equals 1 for $t > 0$ and $-1$ for $t < 0$. Application of the Fourier transform leads to

$$\mathfrak{F}\{h(t)\} = \frac{1}{2\pi}\mathfrak{F}\{\text{sign}(t)\} * \mathfrak{F}\{h(t)\}$$
$$H(j\omega) = \frac{1}{j\pi} \fint \frac{H(j\omega')}{\omega - \omega'}d\omega' \quad (4)$$

where the integral is defined according to the Cauchy's principal value

$$\fint = \lim_{\epsilon \to 0^+} \left[ \int_{-\infty}^{\omega-\epsilon} + \int_{\omega+\epsilon}^{+\infty} \right]. \quad (5)$$

If we separate now the real and the imaginary part of (4) we get

$$U(\omega) = \frac{1}{\pi} \fint \frac{V(\omega')}{\omega - \omega'}d\omega' \quad (6a)$$

$$V(\omega) = -\frac{1}{\pi} \fint \frac{U(\omega')}{\omega - \omega'}d\omega' \quad (6b)$$

where $H(j\omega) = U(\omega) + jV(\omega)$. These equations are known as Kramers–Krönig dispersion relations or Hilbert transform and hold if and only if (2) is satisfied, as proved in [14]. Therefore, they are the frequency domain condition for the causality of a LTI system. We reinterpret now the above relations under a slightly different standpoint. Equation (4) can be seen as the application of a (Hilbert-transform) *reconstruction operator* $\mathcal{R}_0$

$$H_0(j\omega) = \mathcal{R}_0 H(j\omega) = \frac{1}{j\pi} \fint \frac{H(j\omega')}{\omega - \omega'}d\omega'. \quad (7)$$

This operator maps any causal frequency response onto itself
$$H(j\omega) \text{ causal} \Leftrightarrow H_0(j\omega) = \mathcal{R}_0 H(j\omega) = H(j\omega)$$
$$(8)$$

equivalently, $\mathcal{R}_0$ becomes the identity operator when applied to causal responses. If instead we release the causality assumption

on $H(j\omega)$, we obtain $H_0(j\omega) \neq H(j\omega)$, with a corresponding *reconstruction error*

$$\Delta_0(j\omega) = H_0(j\omega) - H(j\omega). \tag{9}$$

A nonvanishing reconstruction error indicates the presence of causality violations in the original frequency response. This will be the main numerical tool that we will further develop for causality detection and characterization.

### C. Practical Difficulties With Dispersion Relations

Two main difficulties arise when trying to apply (7). First, the high-frequency behavior of $H(j\omega)$ for lumped or distributed networks may not be decreasing to zero. It may not even be bounded, as in the case of impedance/admittance representations. This implies difficulties in the definition of the Hilbert transform integral, which holds only when $H(j\omega)$ is square integrable [14].

Even if the Hilbert transform integral is well defined, a second practical problem must be faced in its numerical evaluation. In fact, in practical applications the frequency response is obtained either via numerical simulation or direct measurement and is available only over a set of discrete frequency samples up to a maximum frequency $\omega_{\max}$

$$H(j\omega_k), \quad k = 1, \ldots, K, \quad \omega_K = \omega_{\max}. \tag{10}$$

We can further distinguish between the baseband case

$$\omega_1 = 0 \tag{11}$$

and the bandpass case

$$\omega_1 = \omega_{\min} > 0 \tag{12}$$

with missing samples at low frequencies. In the following, we will focus on the baseband case (11), and we will denote the frequency range where data points are available as

$$\Omega = [-\omega_{\max}, \omega_{\max}], \tag{13}$$

with data for negative frequencies being recovered from basic spectrum symmetries. Full details on the bandpass case will be presented in the Appendix. Under these conditions, the usefulness of dispersion relations is subject to the availability of a robust and efficient algorithm for their numerical computation. This is a challenging task because of two reasons:

- Since the available data span a limited frequency range, the integrals in (6) have to be restricted to $\Omega$, introducing a *truncation error*. Unfortunately, this error may be very large. In order to overcome this issue and achieve a high accuracy, a more advanced form of dispersion relations will be introduced in Section III.
- The discrete nature of the available data introduces a *discretization error* in the numerical evaluation of (6). Also, a dedicated quadrature algorithm must be devised due to the presence of the singular kernel $(\omega - \omega')^{-1}$, since standard techniques may lead to very poor accuracies.

To show the significance of these two errors, we numerically computed the dispersion relations (7) for the $S_{11}$ parameter of a
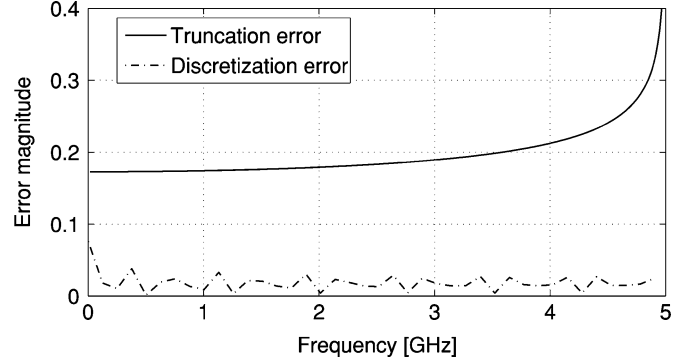


Fig. 1. Numerically computed reconstruction error for the $S_{11}$ coefficient of a simple transmission line (per-unit-length parameters $\mathfrak{L} = 4.73$ nH/cm, $\mathfrak{C} = 3.8$ pF/cm, $\mathfrak{R} = 0.8\ \Omega/\text{cm}$, $\mathfrak{G} = 0$, length $l = 10$ cm), tabulated up to 5 GHz (40 points). The contributions of truncation and discretization errors are shown separately.

simple transmission line, tabulated from 0 up to 5 GHz at 40 frequency points. The numerical computation of the integral in (7) was performed with a conventional quadrature algorithm (trapezoidal rule), regardless of the singular nature of the integral. The integration interval was restricted to the available bandwidth $[-5, 5]$ GHz. Since the $S_{11}$ parameter is certainly causal, we would expect (8) to be satisfied, or equivalently, the reconstruction error $\Delta_0(j\omega)$ to be vanishing. Numerical results are very different. As depicted in Fig. 1, the numerically computed reconstruction error is very large, because of both truncation and discretization errors. Although the discretization error can be somewhat controlled by a sufficiently fine frequency sampling, the truncation error can be very large. This strongly limits the usefulness of dispersion relations, unless a more careful formulation and implementation is devised. This is the subject of the next Section.

## III. GENERALIZED DISPERSION RELATIONS

### A. Dispersion Relations With Subtractions

The main limitation of standard Kramers–Krönig relations (6) is their sensitivity to the high frequency data, which are not available in practice. To overcome this serious issue, the use of a generalized formulation of dispersion relations named *dispersion relations with subtractions* [15], [16] has been proposed in [17], [18]

$$\begin{aligned} H_n(j\omega) &= \mathcal{R}_n H(j\omega) \\ &= \mathcal{L}_H(j\omega) + \frac{\prod_{q=1}^{n}(\omega - \bar{\omega}_q)}{j\pi} \\ &\quad \times \int \frac{H(j\omega') - \mathcal{L}_H(j\omega')}{\prod_{q=1}^{n}(\omega' - \bar{\omega}_q)} \frac{d\omega'}{\omega - \omega'} \end{aligned} \tag{14}$$

where the so-called *subtraction points* $\{\bar{\omega}_q\}_{q=1}^{n}$ are spread over the available bandwidth $\Omega$. In (14), the term $\mathcal{L}_H(j\omega)$ denotes the Lagrange interpolation polynomial [19] for $H(j\omega)$

$$\mathcal{L}_H(j\omega) = \sum_{q=1}^{n} H(j\bar{\omega}_q) \prod_{\substack{p=1 \\ p \neq q}}^{n} \frac{\omega - \bar{\omega}_p}{\bar{\omega}_q - \bar{\omega}_p} \tag{15}$$

with the substraction points $\{\bar{\omega}_q\}_{q=1}^{n}$ used as interpolation knots. A complete derivation of these formulas can be found in

[15], [16]. Here, we just observe that (14) can be interpreted as the application of (4) to the auxiliary frequency response

$$G(j\omega) = \frac{H(j\omega) - \mathcal{L}_H(j\omega)}{\prod_{q=1}^{n}(\omega - \bar{\omega}_q)} \quad (16)$$

which is constructed by subtracting the polynomial trend $\mathcal{L}_H(j\omega)$ from $H(j\omega)$ and dividing by the polynomial normalization factor at the denominator. Note that the singularities of $G(j\omega)$ at the subtraction points are only apparent, due to the presence of the Lagrange polynomial $\mathcal{L}_H(j\omega)$, which equals $H(j\omega)$ for $\omega = \bar{\omega}_q$.

Equation (14), also known as *generalized Hilbert transform* [20], defines a generalized reconstruction operator $\mathcal{R}_n$. Clearly, (7) can be obtained as a particular case of (14) by setting $n = 0$. Similarly, we can define the real operators $\mathcal{R}'_n$, $\mathcal{R}''_n$ that generalize (6) by extracting the real and the imaginary parts of (14)

$$V_n(\omega) = \mathcal{R}'_n U(\omega)$$
$$U_n(\omega) = \mathcal{R}''_n V(\omega) \quad (17)$$

where $H_n(j\omega) = U_n(\omega) + jV_n(\omega)$. As for (7), we have that only causal frequency responses are mapped onto themselves by the reconstruction operator $\mathcal{R}_n$, i.e.,

$$H(j\omega) \text{ causal} \Leftrightarrow H_n(j\omega) = \mathcal{R}_n H(j\omega) = H(j\omega). \quad (18)$$

The generalized reconstruction operator $\mathcal{R}_n$ has two important advantages with respect to $\mathcal{R}_0$. First advantage is generality, since $\mathcal{R}_n$ results well defined for any frequency response having a polynomial growth up to $\omega^{n-1}$. Second, its sensitivity to the high-frequency behavior of $H(j\omega)$ results drastically reduced. This is essentially due to the presence of the polynomial at the denominator in (14), which acts as a sort of "low-pass" filter. These considerations are made more precise in the following.

### B. Truncation Error

Integration in (14) is performed over the whole real line. However, application to bandlimited responses imposes a restriction of the integration interval to $\Omega$ defined in (13). Therefore, only an approximation $\widehat{H}_n(j\omega)$ of the reconstructed frequency response can be evaluated, for $\omega \in \Omega$, as

$$\widehat{H}_n(j\omega) = \mathcal{L}_H(j\omega)$$
$$+ \frac{\prod_{q=1}^{n}(\omega - \bar{\omega}_q)}{j\pi} \int_{\Omega} \frac{H(j\omega') - \mathcal{L}_H(j\omega')}{\prod_{q=1}^{n}(\omega' - \bar{\omega}_q)} \frac{d\omega'}{\omega - \omega'}$$
$$+ \underbrace{\frac{\prod_{q=1}^{n}(\omega - \bar{\omega}_q)}{j\pi} \int_{\Omega^C} \frac{-\mathcal{L}_H(j\omega')}{\prod_{q=1}^{n}(\omega' - \bar{\omega}_q)} \frac{d\omega'}{\omega - \omega'}}_{C_n(j\omega)}.$$
$$(19)$$

The last term includes the contribution of the Lagrange interpolation polynomial $\mathcal{L}_H(j\omega)$ over the complement set $\Omega^C = \mathbb{R}\backslash\Omega$ that identifies the band which is not spanned by the data. If this contribution is not included in the computation, the result turns out to be very inaccurate, thus wasting the effort in using the more sophisticated generalized dispersion relations. Since

the Lagrange polynomial is known analytically, the quantity $C_n(j\omega)$ can be evaluated in closed form and reads

$$C_n(j\omega) = \sum_{q=1}^{n} \frac{H(j\bar{\omega}_q)}{j\pi} \left[\mathbb{L}(\omega) - \mathbb{L}(\bar{\omega}_q)\right] \prod_{\substack{p=1 \\ p \neq q}}^{n} \frac{\omega - \bar{\omega}_p}{\bar{\omega}_q - \bar{\omega}_p},$$
$$(20)$$

where

$$\mathbb{L}(x) = \ln\left|\frac{\omega_{\max} + x}{\omega_{\max} - x}\right|. \quad (21)$$

The expression (20) will be used for the numerical evaluation of (19) in Section III-E. We now define the truncation error $E_n(j\omega)$ by taking the difference between the bandlimited approximation (19) and (14)

$$E_n(j\omega) = \widehat{H}_n(j\omega) - H_n(j\omega)$$
$$= \frac{\prod_{q=1}^{n}(\omega - \bar{\omega}_q)}{j\pi} \int_{\Omega^C} \frac{-H(j\omega')}{\prod_{q=1}^{n}(\omega' - \bar{\omega}_q)} \frac{d\omega'}{\omega - \omega'}.$$
$$(22)$$

This error is a function of number and position of subtraction points. A careful selection of these parameters allows to control this error almost up to arbitrary precision. In fact, when the number of subtractions $n$ is increased, a smaller integrand is obtained in (22), resulting in a smaller truncation error $E_n(j\omega)$. It turns out that a rigorous bound for $E_n(j\omega)$ can be formally derived from (22). Under the hypothesis

$$|H(j\omega)| \leq M|\omega^{\alpha}| \text{ for } \omega \in \Omega^C \quad (23)$$

and for $\alpha = 0, 1, 2, \ldots$, it can be proved (see Appendix B) that

$$|E_n(j\omega)| \leq T_n(\omega) \quad (24)$$

where

$$T_n(\omega) = \frac{M}{\pi} \sum_{q=1}^{n} (\bar{\omega}_q)^{\alpha} \left[\left|\ln\frac{\omega_{\max} - \bar{\omega}_q}{\omega_{\max} - \omega}\right|\right.$$
$$\left. - (-1)^{\alpha+n}\left|\ln\frac{\omega_{\max} + \bar{\omega}_q}{\omega_{\max} + \omega}\right|\right] \times \prod_{\substack{p=1 \\ p \neq q}}^{n} \frac{|\omega - \bar{\omega}_p|}{\bar{\omega}_q - \bar{\omega}_p} \quad (25)$$

and that this bound is tight. The case $\alpha = 0$, $M = 1$ is particularly important since it corresponds to the scattering responses of passive networks, for which we have $|H(j\omega)| \leq 1$. From (25) we can easily verify that the truncation error is bounded between any pair of subtraction points and decreases when their number $n$ is increased. Fig. 2 confirms these statements by depicting the truncation error bound $T_n(\omega)$ for $n = 4, 8, 12$.

### C. Optimal Displacement of Subtraction Points

The truncation error is frequency-dependent. It vanishes at the subtraction points, and it reaches a maximum between each pair of subtractions. The exact values of these maxima depend on the actual location of the subtraction points. It is clear that an optimal placement of these points is obtained when all these maxima are equal, so that the truncation error can be uniformly bounded by a constant throughout the bandwidth of interest. Such condition is approximately reached when the subtraction
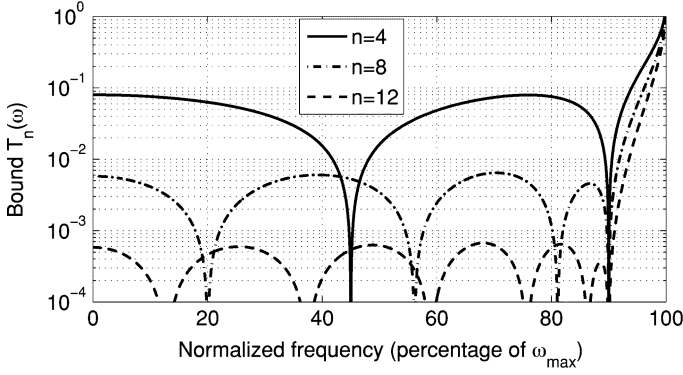
Fig. 2. Truncation error bound (for $\alpha = 0$, $M = 1$) as a function of the number $n$ of subtraction points.
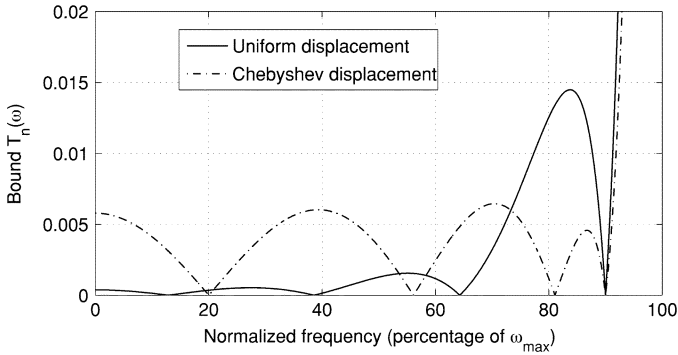


Fig. 3. Truncation error bound for uniform and Chebyshev distributions of $n = 8$ subtraction points ($\alpha = 0, M = 1$).

frequencies $\{\bar{\omega}_q\}_{q=1}^n$ are placed according to a Chebyshev distribution [10]

$$\bar{\omega}_q = -\omega_{\max}(1 - \epsilon)\cos\frac{(q - 1)\pi}{n - 1}, \quad q = 1, \ldots, n. \quad (26)$$

This placement allows to minimize the truncation error bound uniformly in the bandwidth

$$\Omega' = [-\omega_{\max}(1 - \epsilon), \omega_{\max}(1 - \epsilon)] \quad (27)$$

i.e., in the full bandwidth $\Omega$ except two arbitrarily small intervals at the bandwidth edges. Obviously, the truncation error diverges at the bandwidth edges due to the missing out-of-band samples. A comparison between the truncation error for uniform and Chebyshev distributions is depicted in Fig. 3. An intuitive justification for this result can be given noting that the truncation error increases when the Hilbert kernel gets close to the edges. Therefore, an increased density of subtractions near the edges guarantees a smaller truncation error. The optimal displacement of subtraction points for the bandpass case (12) is discussed in Appendix A.

### D. Discretization Error

We focus now on the unavoidable discretization error arising in the numerical evaluation of (19) via some quadrature rule. We denote as $\widetilde{H}_n(j\omega)$ the outcome from a given numerical quadrature rule of order $\nu$, whereas $D_n(j\omega)$ denotes the corresponding discretization error

$$D_n(j\omega) = \widetilde{H}_n(j\omega) - \widehat{H}_n(j\omega). \quad (28)$$

The discretization error may be very large if no special care is taken in handling the singular kernel of the Hilbert transform. To regularize the integral, we adopt a singularity extraction procedure. The singular part of the integrand function is subtracted from the integral and added separately, as shown in the following equation:

$$\fint_\Omega g(\omega')\frac{d\omega'}{\omega - \omega'}$$
$$= \int_\Omega [g(\omega') - g(\omega)]\frac{d\omega'}{\omega - \omega'}$$
$$+ g(\omega)\fint_\Omega \frac{d\omega'}{\omega - \omega'}$$
$$= \int_\Omega \frac{g(\omega') - g(\omega)}{\omega - \omega'}d\omega' + g(\omega)\mathbb{L}(\omega). \quad (29)$$

The second term in (29) represents the contribution of the singularity and is evaluated in closed form using (21). The remaining integral is smooth and well behaved, since the integrand function is now regular for $\omega' = \omega$ and can be computed with any quadrature routine.

In order to estimate the discretization error introduced by numerical integration, one can opt for two different strategies, depending on the application. The first strategy performs the computation twice using two different integration methods with different orders $\nu_1 < \nu_2$. An estimate of the discretization error is obtained by taking the difference of the two results

$$\widetilde{D}_n(\omega) = \left|\widetilde{H}_n^{\nu_1}(j\omega) - \widetilde{H}_n^{\nu_2}(j\omega)\right| \simeq |D_n(j\omega)| \quad (30)$$

under the reasonable assumption that the higher order quadrature rule provides a much better result, which can be used as the reference for the error estimate.

The above technique usually gives reasonable estimates but does not provide an upper bound of the discretization error. A possible alternative is to derive a worst-case bound for the adopted quadrature rule. As an example, conservative bounds for the Simpson's quadrature rule have been derived in [21]. Using this second strategy will guarantee that the actual discretization error is always smaller than the error bound. The specific choice depends whether one prefers the results with the highest resolution (first strategy) or the worst-case scenario (second strategy). The latter will guarantee that no false positives are obtained in the causality test, to be presented in Section IV.

Without any a priori information, a low-order quadrature rule is preferable in order to build a robust numerical tool which is applicable also to noisy data. Throughout this work, we use a combination of Simpson's and trapezoidal rule, using (30) to estimate the discretization error.

### E. Error-Controlled Evaluation of Dispersion Relations

The numerically reconstructed frequency response $\widetilde{H}_n(j\omega)$ defined via the generalized dispersion relations is obtained by applying (19) to the set of discrete samples in (10). The first term in (19) is the Lagrange interpolation polynomial and is analytically known, see (15). The integral in the second term is computed using the singularity extraction procedure (29) com-

bined with some quadrature rule. Finally, the last term in (19) is also known analytically and is given by (20).

Thanks to the systematic analysis of truncation and discretization errors, the worst-case error $E_n^{\text{tot}}(\omega)$ affecting the numerical result

$$|\widetilde{H}_n(j\omega) - H_n(j\omega)| \leq E_n^{\text{tot}}(\omega) \qquad (31)$$

is known and is given by

$$E_n^{\text{tot}}(\omega) = T_n(\omega) + \widetilde{D}_n(\omega). \qquad (32)$$

In addition, the accuracy in the reconstruction can be greatly enhanced by increasing the number of subtraction points $n$, thus lowering $E_n^{\text{tot}}(\omega)$ down to the limit represented by discretization error $\widetilde{D}_n(\omega)$. The excellent accuracy of the proposed technique is demonstrated in the applications presented in the next Sections.

### F. Comparison With Existing Techniques

Before proceeding any further, we compare our approach with previous works on dispersion relations, to show how the state of the art is improved.

- In [5] and [10] the truncation error is minimized with an extrapolation of the available data beyond the maximum available frequency $\omega_{\max}$. This may somehow improve the accuracy of the result, but does not allow neither a rigorous arbitrary minimization nor an estimation of the truncation error, as guaranteed by the proposed approach.
- Some earlier works on dispersion relations with subtractions [11], [10] neglect the Lagrange polynomial $\mathcal{L}_H(j\omega)$ under the integral sign in (14). Unfortunately, without that term the integrand function in (14) turns out to be singular for $\omega = \bar{\omega}_q$, therefore its numerical evaluation can be inaccurate. This approximation might be acceptable only in very particular cases. For example, in case of highly resonant data as in [11] and [10], the subtraction points $\{\bar{\omega}_q\}$ can be placed where $H(j\omega)$ is small, resulting in a small interpolation polynomial $\mathcal{L}_H(j\omega)$. It is clear that this solution lacks generality and significantly limits the number and position of subtractions.
- In [3] and [22], the integration interval in (14) is simply restricted to available bandwidth $\Omega$ without any special care. This approach introduces large error terms, called "artifacts" in [3] and [22], which may compromise the benefits of adopting a generalized form of dispersion relations. We introduce instead (19), a new bandlimited version of (14), that includes the additional term $C_n(\omega)$, related to the out-of-band contribution of the Lagrange polynomial, which is extracted analytically. Only when this term is included one can rigorously prove that the truncation error (22) is bounded by (25) and can be arbitrarily minimized by increasing $n$. Fig. 4 displays how neglecting the term $C_n(\omega)$ in (19) increases the recontruction error beyond the bound (25). If $C_n(j\omega)$ is instead considered the reconstruction error always remains below the predicted bound.
- We finally cite the interesting work [9] that derives rigorous bounds for the reconstruction error, with application to the
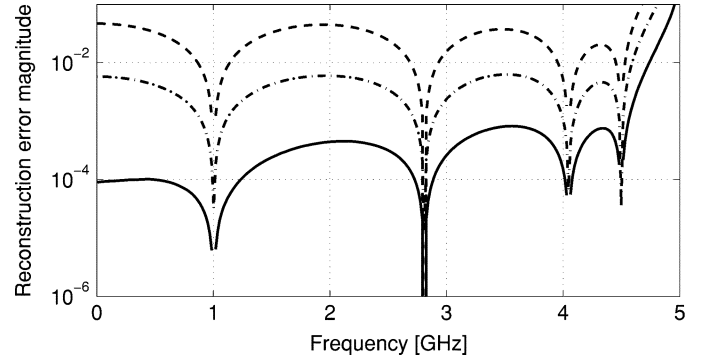


Fig. 4. Magnitude of the reconstruction error for the transmission line insertion loss $S_{11}$ of Fig. 1, obtained when the term $C_n(j\omega)$ in (19) is either considered (solid line, our approach), or neglected (dashed line, as in [3] and [22]). The truncation error bound $T_n(\omega)$ is also depicted (dashed–dotted line).

dielectric permittivity and magnetic permeability. The approach is quite different from ours, and based on the properties of Stieltjes functions. The functions considered in [9] have finite limit for $\omega \to \infty$ and not a generic polynomial growth, as considered in this paper. An extension of [9] to this kind of functions is an interesting direction for future research on the topic, and will allow a comparison with the proposed approach.

## IV. ROBUST CAUSALITY CHECK FOR TABULATED DATA

Measurement or simulation errors may destroy the causality of tabulated frequency responses, otherwise guaranteed by physical reasons. As documented in [17] and [23] even small causality violations in the data may seriously compromise modeling and simulation tasks, due to the physical inconsistency of the flawed frequency samples. Therefore, a robust and accurate procedure for causality verification of tabulated frequency data is highly desirable, in order to certify a given dataset for safe use in a CAD environment.

One possibility to infer causality from frequency-domain responses is to directly check condition (2) by computing the inverse Fourier transform of (10) via fast Fourier transform (FFT). This procedure turns out to be very unreliable. In fact, the bandlimited nature of the data may give rise to the well-known Gibbs phenomenon and to aliasing effects [5], which superimpose to the true impulse response $h(t)$ a significative error term, thus distorting the causality check. Using the standard dispersion relations (4) is also unreliable, due to the possibly large truncation error in the evaluation of the Hilbert transform. In this section, we present an accurate and reliable method to ascertain the causality of tabulated data, based on the generalized dispersion relations.

### A. Theoretical Derivation

A given frequency response $H(j\omega)$ is causal if and only if the ideal reconstruction error

$$\Delta_n(j\omega) = H_n(j\omega) - H(j\omega) \qquad (33)$$

is vanishing at all frequencies. However, in practice only the numerical estimate

$$\widetilde{\Delta}_n(j\omega) = \widetilde{H}_n(j\omega) - H(j\omega)$$
$$= \Delta_n(j\omega) + E_n(j\omega) + D_n(j\omega) \qquad (34)$$

is available, differing from the ideal case because of truncation and discretization errors. In order to unbias the causality test from these terms and obtain a reliable identification of causality violations, we explicitly take into account the bound in (32). Two situations may occur.

When

$$\exists k: \quad |\widetilde{\Delta}_n(j\omega_k)| > E_n^{\text{tot}}(\omega_k) \qquad (35)$$

we are confident that $H(j\omega)$ is not causal, because the computed reconstruction error exceeds the bound that has been derived for all possible sources of numerical errors. When

$$|\widetilde{\Delta}_n(j\omega_k)| \leq E_n^{\text{tot}}(\omega_k) \quad \forall k \qquad (36)$$

any causality violation in the data is smaller than the numerical resolution affecting the calculations, hence it cannot be detected. Some control over the resolution is provided by the number of subtraction points $n$, as discussed below. However, this resolution cannot be made arbitrarily small, being intrinsically limited by the finite number of frequency samples, known over a finite bandwidth.

We now provide some insight on the effectiveness of (35) in the detection of causality violations. To this end, we assume that the available data for $H(j\omega)$ are composed by the true frequency response $H_c(j\omega)$, which is certainly causal, and a perturbation term $P(j\omega)$

$$H(j\omega) = H_c(j\omega) + P(j\omega). \qquad (37)$$

This perturbation may be due, e.g., to measurement or simulation errors during the extraction of the raw frequency responses. Therefore, we define $P(j\omega)$ as identically vanishing outside the available bandwidth. In general, we can split this perturbation as

$$P(j\omega) = P_c(j\omega) + P_a(j\omega) \qquad (38)$$

where $P_c(j\omega)$ is causal and $P_a(j\omega)$ is anti-causal, i.e., having an inverse Fourier transform $p_a(t) = \mathfrak{F}^{-1}\{P_a(j\omega)\}$ which is vanishing for $t \geq 0$. Applying now (33) and (34) to (37), and noting that the ideal reconstruction error for both $H_c(j\omega)$ and $P_c(j\omega)$ is vanishing, we get the following expression for the numerically computed reconstruction error

$$\widetilde{\Delta}_n(j\omega) = 2[\mathcal{L}_{P_a}(j\omega) - P_a(j\omega)] + E_n(j\omega) + D_n(j\omega). \qquad (39)$$

The above expression takes into account that any anti-causal function satisfies $p_a(t) = -\text{sign}(t)p_a(t)$, which leads to anti-

causal dispersion relations identical to (14), except for a sign change in front of the integral. Since

$$|\widetilde{\Delta}_n(j\omega)| \geq 2|P_a(j\omega) - \mathcal{L}_{P_a}(j\omega)|$$
$$- |E_n(j\omega) + D_n(j\omega)|$$
$$\geq 2|P_a(j\omega) - \mathcal{L}_{P_a}(j\omega)| - E_n^{\text{tot}}(\omega)$$

our proposed test (35) will detect the causality violation when the following condition holds

$$\exists k: \quad |P_a(j\omega_k) - \mathcal{L}_{P_a}(j\omega_k)| > E_n^{\text{tot}}(\omega_k). \qquad (40)$$

This expression involves only the anti-causal perturbation term and its associated Lagrange polynomial. In (40), the left-hand side can be interpreted as the effective causality violation "seen" by the algorithm, while the right-hand side as its "resolution." Obviously, detection occurs when the violation is greater than the resolution $E_n^{\text{tot}}(\omega)$, which is given by (32). Increasing the number of subtractions $n$ improves the detection capabilities of the method because the truncation error $T_n(\omega)$ is decreased, thus enhancing the resolution up to the limit represented by the discretization error $\widetilde{D}_n(\omega)$.

There is only one situation when a large number of subtractions does not lead to any advantage. This case occurs when $|P_a(j\omega) - \mathcal{L}_{P_a}(j\omega)|$ decreases with $n$ faster than the truncation error, i.e., when the causality violation $P_a(j\omega)$ is very smooth. Standard Fourier analysis arguments show that the corresponding time-domain representation $p_a(t)$ has a narrow support or a fast decay rate away from $t = 0$. Such violation is intrinsically difficult to detect, independently on the adopted algorithm. Finally, we remark that the error bound (25) that we derived is the strictest possible (see Appendix B), and it provides the best resolution with a given bandwidth.

### B. Example: Detection of Weak Causality Violations

We verified the above considerations with the following example, which highlights also the excellent resolution of the proposed method. The $S$-parameters of the line considered in Fig. 1 have been perturbed with a Gaussian-shaped term

$$P(j\omega) = A \exp\left\{-\left(\frac{\omega - \omega_0}{2\pi B}\right)^2\right\} \qquad (41)$$

centered at $\omega = \omega_0$. The above perturbation is obviously noncausal, with $A$ and $B$ controlling respectively the amplitude and bandwidth of the induced causality violation. We applied the proposed causality check in order to detect this violation. In Fig. 5, the norm[1] of both frequency-dependent threshold $\|E_n^{\text{tot}}(\omega)\|_\infty$ and reconstruction error $\|\widetilde{\Delta}_n(\omega)\|_\infty$ are plotted versus the number of subtractions $n$, for different perturbation amplitudes $A$. Detection occurs when $\|\widetilde{\Delta}_n(\omega)\| > \|E_n^{\text{tot}}(\omega)\|$, i.e., when the solid curve emerges from the dashed one. As evident from the top panel, even very weak causality violations can be revealed by increasing the number of subtractions, due to the reduction of the detection threshold $E_n^{\text{tot}}(\omega)$. In the

---

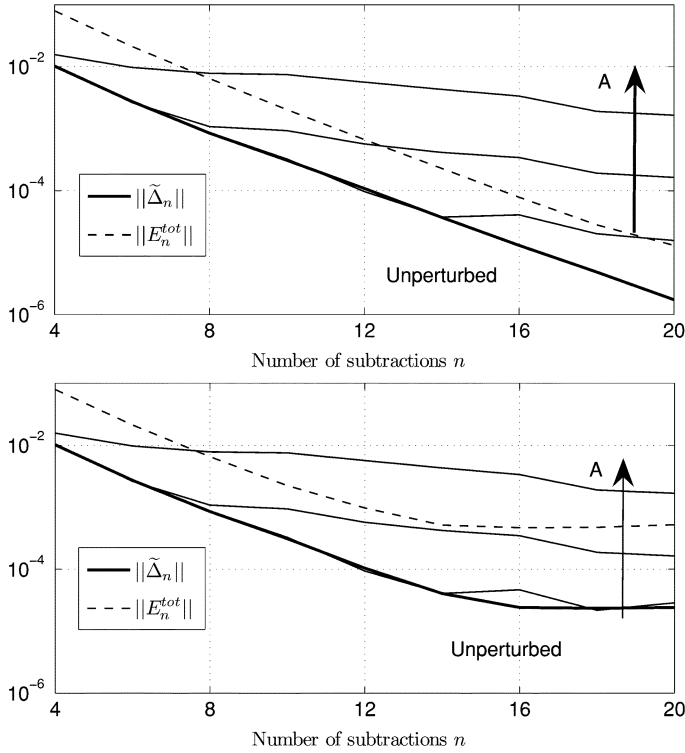[1]The adopted $\infty$-norm is defined as $\| \cdot \|_\infty = \max_{\Omega'} | \cdot |$ with $\Omega'$ given by (27).

Fig. 5.   Norm of the frequency-dependent threshold $\|E_n^{\text{tot}}(\omega)\|_\infty$ and of the reconstruction error $\|\widetilde{\Delta}_n(\omega)\|_\infty$ versus the number of subtractions $n$. The perturbation is centered at $f_0 = 2.5$ GHz, has a semi-bandwidth $B = 0.5$ GHz, and different amplitudes $A = 10^{-2}, 10^{-3}, 10^{-4}$. The thickest solid line denotes the unperturbed case $(A = 0)$. The $S$-parameters of the line have been computed at 1000 points (top panel) and 250 points (bottom panel).
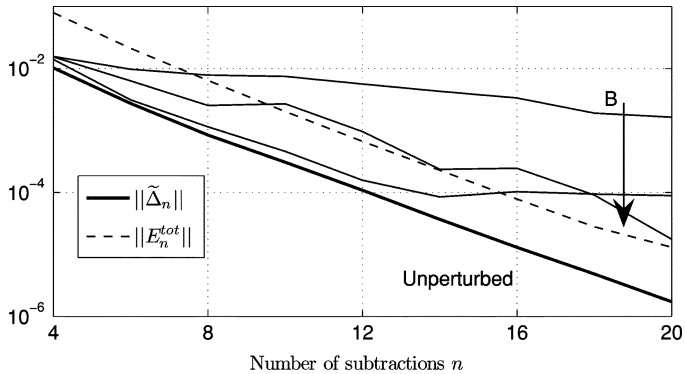


Fig. 6.   As in the top panel of Fig. 5, but with constant perturbation amplitude $A = 10^{-3}$ and variable perturbation bandwidth $B = 0.5, 1, 1.5$ GHz.

bottom panel the available frequency points have been reduced from 1000 to 250. The increased discretization error limits the reduction of $\|E_n^{\text{tot}}(\omega)\|$ to about $5 \times 10^{-4}$. Therefore, the detection of causality violations smaller than this baseline is not possible.

We focus now on the effect of the perturbation bandwidth $B$ on the causality check. If $B$ increases, the perturbation becomes wider and smoother in the frequency domain, and narrower in the time domain. As discussed above, such a causality violation is intrinsically harder to be detected, as confirmed by the curves depicted in Fig. 6.
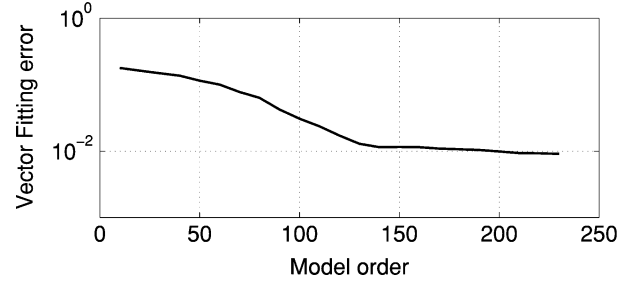


Fig. 7.   Model extraction from measured scattering data of a long interconnect. The residual error of the rational model generated by VF is plotted versus model order.
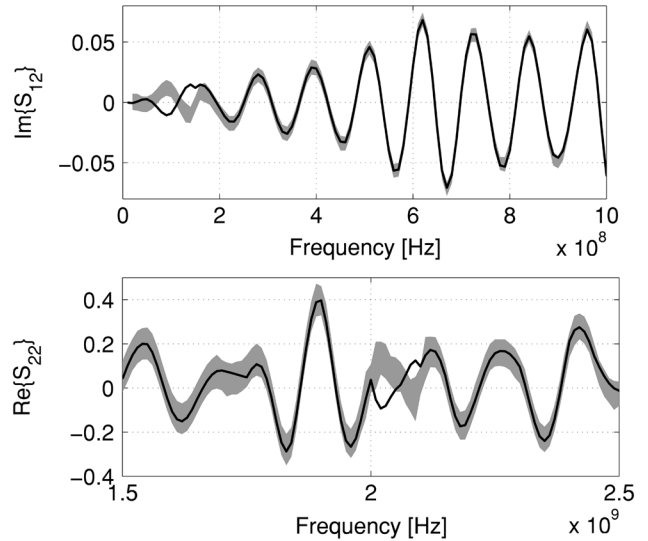


Fig. 8.   Measured raw data (solid lines) and corresponding numerical reconstruction with associated worst-case error bar (gray shaded areas) for the $S_{12}$ (top panel) and $S_{22}$ (bottom panel) scattering parameters of a long interconnect link.

### C. Example: Qualification of a Measured Dataset

We consider here a long interconnect link, whose scattering parameters have been measured with a VNA in the frequency range 10 MHz–10 GHz (courtesy of IBM). We apply the proposed causality check technique to qualify the measurement results. In fact, we suspect the presence of some inconsistency in this dataset from the failure of a standard macromodeling process. More precisely, we tried to compute with the popular and robust vector fitting (VF) algorithm [24] a model for the dataset. Fig. 7 shows the model error for different orders. Clearly, VF is unable to improve the model accuracy beyond $10^{-2}$, even if the model order is significantly increased.

Application of the proposed methodology indicates the presence of causality violations in the data. In the top panel of Fig. 8, the imaginary part of the $S_{12}$ parameter is depicted (solid line), together with its numerical reconstruction computed from the real part via dispersion relations. The latter is depicted in the plot with a gray shaded area, in order to take into account that the numerical reconstruction is only available with an associated numerical error. The thickness of the shaded area is related to the worst case error (32). The points which fall outside of this region are inconsistent because they do not respect (36). Small

causality violations have been found also in other scattering parameters, as shown in the bottom panel of Fig. 8 for $S_{22}$. As demonstrated in [23], causality violations in the raw data may seriously compromise the accuracy and convergence speed of VF. This happens because VF, while minimizing iteratively the error between the estimated macromodel and the given data, enforces the model poles to be in the left half plane. As shown in [23], this enforces both the model stability and causality. However, when the raw frequency data are not causal, this is an impossible task, since the frequency response of a macromodel that is *causal* by construction will never match with good accuracy *noncausal* data. More details on this issue, including the related theoretical background, can be found in [23].

## V. ROBUST PASSIVITY CHECK FOR TABULATED DATA

Passive components such as lumped elements (capacitors, resistors, inductors) and interconnect structures (wires, connectors, board and package lines) are unable to generate energy. However, when the frequency response of a passive component or subsystem is obtained through a measurement or a simulation, errors may compromise the passivity of the data, thus impairing the accuracy and the physical consistency of the characterization. Moreover, CAD models derived from non-passive data may be non-passive too, leading to wrong and divergent simulations results, as well documented in the literature [25], [23]. A passivity check procedure is therefore important to qualify frequency datasets for safe use in CAD design tools.

### A. Theoretical Derivation

The basic passivity conditions for $S$-parameters are given by the following theorem [13], where the scattering matrix $\mathbf{S}(s)$ is considered in the Laplace $s$-domain.

*Theorem 2:* A scattering matrix $\mathbf{S}(s)$ represents a passive system if and only if:
1) each element of $\mathbf{S}(s)$ is analytic[2] in $\mathbb{R}_e\{s\} > 0$;
2) $\mathbf{I} - \mathbf{S}^H(s)\mathbf{S}(s)$ is a nonnegative-definite matrix[3] for all $s$ such that $\mathbb{R}_e\{s\} > 0$;
3) $\mathbf{S}(s^*) = \mathbf{S}^*(s)$.

The superscripts $^*$ and $^H$ denote the complex conjugate and the transpose conjugate, respectively. Since Theorem 2 implies the knowledge of the scattering matrix in the whole $\mathbb{R}_e\{s\} > 0$ half plane, it is not suitable for practical purposes, when $\mathbf{S}(s)$ is available only on the imaginary frequency axis, i.e., for $s = j\omega$. If conditions 2) and 3) are restricted to $s = j\omega$, passivity can be fully ascertained only for lumped stable systems [23]. To remove this strong limitation we exploit the following theorem [13], that holds for both distributed and lumped systems.

*Theorem 3:* A scattering matrix $\mathbf{S}(j\omega)$ represents a passive system if and only if
1) dispersion relations (14) hold for $\mathbf{S}(j\omega)$;
2) $\mathbf{I} - \mathbf{S}^H(j\omega)\mathbf{S}(j\omega)$ is a nonnegative-definite matrix for all $\omega$;

[2]A complex function $F(s)$ is analytic in a given region $\Sigma$ if it has no singularities in $\Sigma$.

[3]A complex hermitian matrix $\mathbf{A} = \mathbf{A}^H$ is nonnegative-definite if $\mathbf{x}^H\mathbf{A}\mathbf{x} \geq 0$ for all complex vectors $\mathbf{x} \neq 0$.
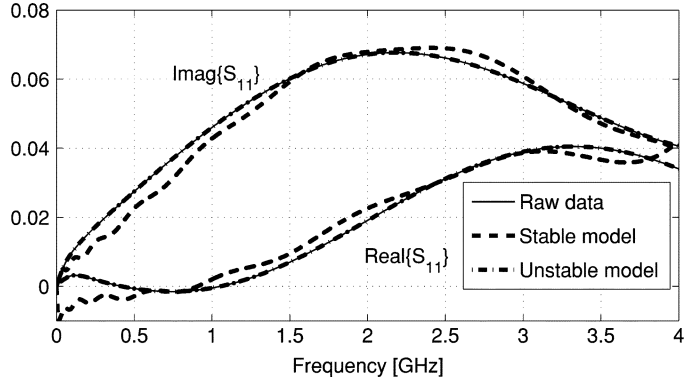


Fig. 9. Return loss $S_{11}$ for a three-conductor transmission line. The results of a field solver (solid lines) are compared to the responses of two different VF-generated models: a model with stable poles only (dashed lines, inaccurate) and a model allowing for unstable poles (dashed–dotted lines, very accurate).

3) $\mathbf{S}(-j\omega) = \mathbf{S}^*(j\omega)$.

In this Theorem, the restriction of conditions 2) and 3) to the imaginary axis is compensated by condition 1), which states that causality is a necessary condition for passivity. Thanks to Theorem 3, we are able to investigate the passivity of a scattering response from its knowledge on the frequency axis only.

Based on this powerful theorem, a numerical passivity test for tabulated data can be established as follows. Condition 1) requires $\mathbf{S}(j\omega)$ to be causal. This condition can be verified with the procedure discussed in Section IV. For condition 2), one simply checks if all the singular values of $\mathbf{S}(j\omega)$ are bounded by one $\forall\omega$. Finally, condition 3) represents the spectrum symmetries valid for the Fourier transform of real valued signals. This condition is always assumed to hold.

### B. Example

We applied the proposed passivity check scheme to the scattering parameters of three coupled lines, computed with an electromagnetic solver up to 4 GHz (courtesy of Nokia). The generation of a good macromodel for this dataset proved to be impossible, even with the robust vector fitting (VF) algorithm. In Fig. 9, the raw frequency data are compared with the response of two different models generated with VF. The first model has been constructed following the standard procedure of rejecting the poles with positive real part. The model is therefore stable but it turns out to be very inaccurate. A satisfactory accuracy could be achieved only with a second model, obtained by VF by releasing the constraint of stable poles. The poles of both models are depicted in Fig. 10, showing that the second model includes poles in the right-hand plane and is therefore nonpassive. In summary, both models are useless, either because of poor accuracy or unstable behavior.

The proposed passivity check scheme was applied in order to track the main reason for these difficulties. First, we verified condition 2) of Theorem 3. Since all singular values of the scattering matrix are uniformly bounded by one (see Fig. 11), this condition is fulfilled. However, the data are not passive because condition 1) is violated, as shown in Fig. 12, where the given $S_{11}$ parameter is compared with its numerical reconstruction computed via dispersion relations. Inconsistencies are clearly visible
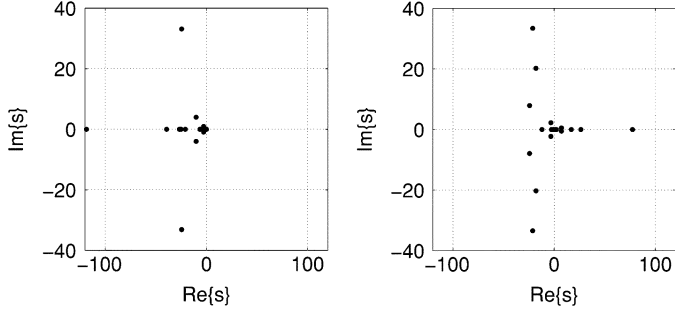
Fig. 10. Poles of the VF-generated models (Grad/s units): stable case (left) and unstable case (right).
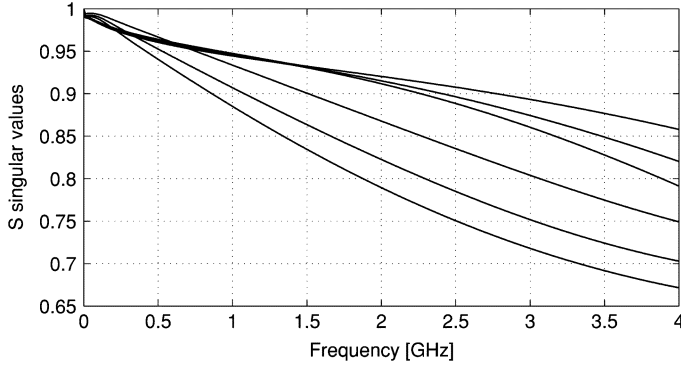


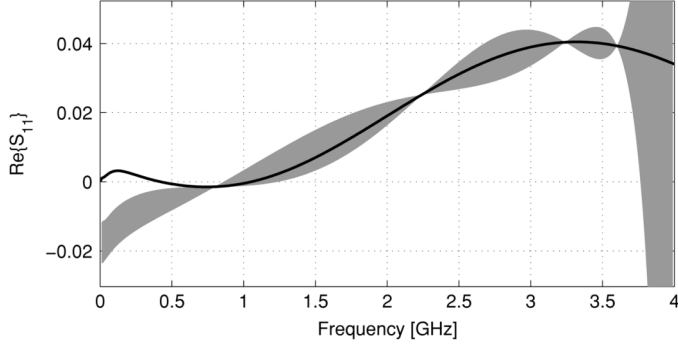Fig. 11. Singular values of the scattering matrix as a function of frequency.



Fig. 12. Causality check result for the $S_{11}$ parameter. Same notation as in Fig. 8.

at low frequency, denoting obvious causality violations. These are indeed the root cause of the modeling problems.

## VI. CAUSALITY-CONSTRAINED INTERPOLATION

In this section, we develop a causality-controlled interpolation scheme based on the generalized dispersion relations. Preliminary results on this scheme were first documented in [26]. The main advantage of the proposed algorithm is a superior accuracy with respect to standard interpolation schemes, with the additional guarantee of the causality in the result. As an application example, we also show the usefulness of this technique in recovering a sound estimate of the system response at missing low-frequency samples, including the dc (zero-frequency) point. It is well known that such points are usually not available via standard measurements or simulations.

### A. Theoretical Derivation

We consider a tabulated frequency response (12) with the aim of reconstructing the missing frequency data for $|\omega| < \omega_{\min}$. This task can be easily accomplished by interpolating the real and imaginary parts of $H(j\omega) = U(\omega) + jV(\omega)$ with, for example, splines. Unfortunately, this simple solution fails to provide a physically consistent result, since the independent reconstruction of the real and imaginary parts does not preserve the relations imposed by causality.

Physical consistency can be achieved by combining interpolation and dispersion relations as follows. First, a reconstructed imaginary part is obtained as

$$\bar{V}_R(\omega) = \mathcal{S}V(\omega) \quad |\omega| < \omega_{\min}, \tag{42}$$

where $\mathcal{S}$ denotes a standard (e.g., linear or spline-based) interpolation scheme using the available samples $V(\omega_k)$. The result differs from the exact but unknown $V(\omega)$ by some interpolation error $\delta V_R(\omega)$

$$\bar{V}_R(\omega) = V(\omega) + \delta V_R(\omega) \quad |\omega| < \omega_{\min}. \tag{43}$$

This reconstructed dataset is used to fill the data gap as

$$V_R(\omega) = \begin{cases} \bar{V}_R(\omega) & |\omega| < \omega_{\min} \\ V(\omega) & \omega_{\min} \leq |\omega| \leq \omega_{\max} \end{cases}. \tag{44}$$

In a second stage, the missing portion of the real part in $[-\omega_{\min}, \omega_{\min}]$ is reconstructed from $V_R(\omega)$ using the generalized dispersion relations. More precisely, if we denote as $\widetilde{\mathcal{R}}_n''$ the numerical discretization of the real reconstruction operator in (17), we define

$$\widetilde{U}_R(\omega) = \widetilde{\mathcal{R}}_n'' V_R(\omega) \quad \omega \in [-\omega_{\min}, \omega_{\min}] \tag{45}$$

The complete reconstructed real part is thus obtained as

$$U_R(\omega) = \begin{cases} \widetilde{U}_R(\omega) & |\omega| < \omega_{\min} \\ U(\omega) & \omega_{\min} \leq |\omega| \leq \omega_{\max} \end{cases}. \tag{46}$$

The reconstructed response

$$H_R(\omega) = U_R(\omega) + jV_R(\omega) \tag{47}$$

is causal by construction regardless of the interpolation error $\delta V_R(\omega)$, since its presence is accounted for in the computation of the real part. In fact, $U_R(\omega)$ includes its generalized Hilbert transform, since

$$\widetilde{U}_R(\omega) = U(\omega) + \widetilde{\mathcal{R}}_n'' \delta V_R(\omega) \quad |\omega| < \omega_{\min}. \tag{48}$$

It must be noted that, although the interpolation error $\delta V_R(\omega)$ vanishes outside $[-\omega_{\min}, \omega_{\min}]$, its Hilbert transform may not. However $\widetilde{\mathcal{R}}_n'' \delta V_R(\omega)$ is very small outside the missing bandwidth, vanishing at all subtraction points. Therefore, it can be considered to be important only in the reconstructed frequency gap $[-\omega_{\min}, \omega_{\min}]$, without significantly affecting the causality of $H_R(j\omega)$.
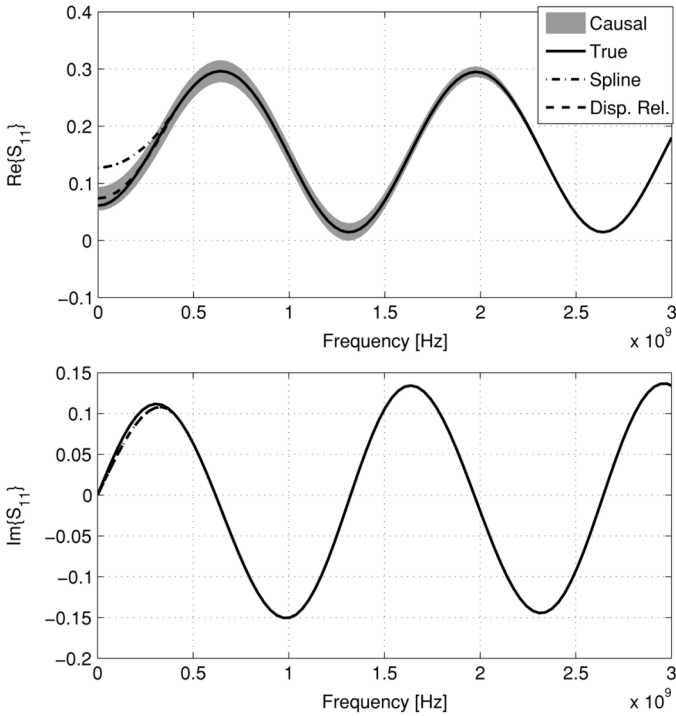
Fig. 13. Exact $S_{11}$ parameter of a transmission line (solid line) is compared with the results of a standard spline-based interpolation (dashed–dotted line) and our proposed causality-constrained interpolation (dashed line). Bounds imposed by causality on the real part are also shown (shaded area).

In order to maximize the accuracy in the missing bandwidth $[-\omega_{\min}, \omega_{\min}]$, a careful placement of the subtraction points is in order. Two conflicting constraints must be considered. On one hand, the subtraction points should be placed close to the edges of the missing bandwidth, so that the truncation error is minimized where needed. On the other hand, any pair of subtraction points should not be too close, since an excessive proximity of singularities in (19) increases the numerical discretization error. We found that the following rule leads to an appropriate placement of subtractions ($n$ is supposed to be even)

$$\{\bar{\omega}_q\}_{q=1}^n = \{\pm\omega_{\min}(1+\beta)^i, i = 1,\dots,n/2\} \qquad (49)$$

with $\beta = 0.2/0.3$. The number of subtractions $n$ is determined using the closed-form bound [25], in order to guarantee a truncation error in the missing bandwidth smaller than any prescribed tolerance.

### B. Analytic Example

We first demonstrate the performance of the proposed technique with an analytic example. We computed the $S_{11}$ parameter of a simple transmission line (per-unit-length parameters: $\mathcal{L} = 5.2$ nH/cm, $\mathcal{C} = 1.1$ pF/cm, $\mathcal{R} = 1.3$ $\Omega$/cm, $\mathcal{G} = 0$, length: $l = 5$ cm) from 0.4 to 10 GHz. Then, we reconstructed $S_{11}$ in the missing bandwidth (from 0 to 0.4 GHz) using a standard spline interpolation for both real and imaginary parts, and the proposed causality-constrained technique. Fig. 13 reports the results. The two interpolations for the imaginary part are identical, whereas the real part estimates are quite different. The proposed technique guarantees a significantly better accuracy and satisfies the bounds imposed by causality (shaded area).
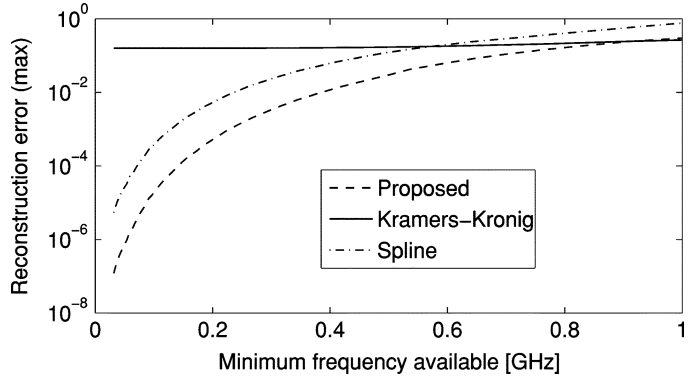


Fig. 14. Maximum error between the reconstructed $S_{11}$ parameter obtained from (47) with respect to the exact value, as a function of missing bandwidth. Results from different interpolation techniques are shown: proposed method (dashed line), proposed with standard Kramers–Krönig relations (solid line) and splines (dashed–dotted line).

Spline interpolation fails to provide both a good accuracy and a causal result.

The sensitivity of the reconstruction with respect to the extent of the data gap was also tested. We varied the amplitude of the missing bandwidth in the range $\omega_{\min} \in [0, 1]$ GHz, and we computed the corresponding interpolation error. Fig. 14 depicts this error as a function of $\omega_{\min}$. This test shows that causality-constrained interpolation is 3–10 times more accurate than conventional algorithms. In the same plot, we also report the poor accuracy that one achieves if Kramers–Krönig relations (6) are blindly used, instead of employing the proposed generalized Hilbert transform operator.

The above results can be interpreted as follows. The causality-constrained interpolation guarantees a better performance since it resorts to interpolation for either the real *or* the imaginary part only, the other one being accurately computed with dispersion relations. Therefore, a careful choice for the part to be interpolated allows a reduction of the interpolation error. For the case of a missing interval located around the zero frequency (dc), it is always convenient to interpolate the imaginary part, since it vanishes for $f = 0$ because of basic spectrum symmetries. This condition provides an additional interpolation point that increases the accuracy. The proposed technique can be also applied to reconstruct data within any arbitrary bandwidth, not necessarily centered at dc. In this case, since there is no *a priori* information on which part should be preferred for interpolation, the only advantage of the proposed scheme is the guarantee of the causality of the result.

### C. Application Example

We consider here a package to package differential link, routed through the first package, a PCB, a connector, another PCB, and then back through to the second package (courtesy of Dr. K. Bois, HP). The scattering parameters of the interconnect were measured with a 4-port vector network analyzer from 10 MHz to 20 GHz. Due to the interconnect length, the parameters have very fast phase variations, as depicted in Fig. 15 for the insertion loss $S_{31}$.

In order to recover the missing dc point, both standard spline interpolation and the proposed scheme were applied. The two results turn out to be quite different, as shown in Fig. 16. This
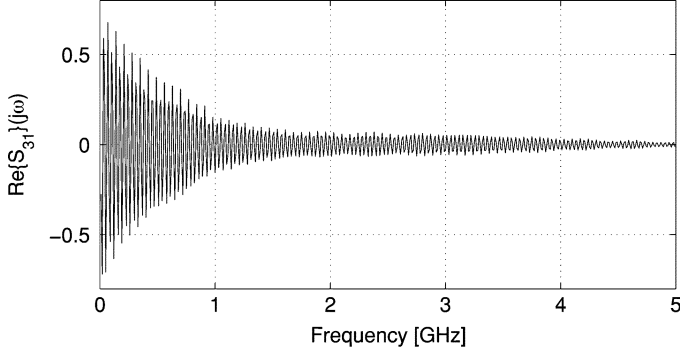
Fig. 15. Insertion loss $S_{31}$ (real part) of the differential I/O link. The frequencies from 5 to 20 GHz are not shown for clarity.
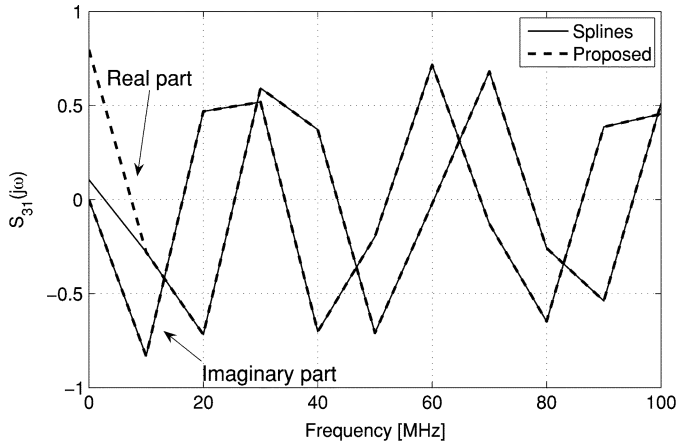


Fig. 16. Insertion loss $S_{31}$ for low frequencies, with the additional dc point estimated by the proposed method (dashed line) and standard spline interpolation (solid line).
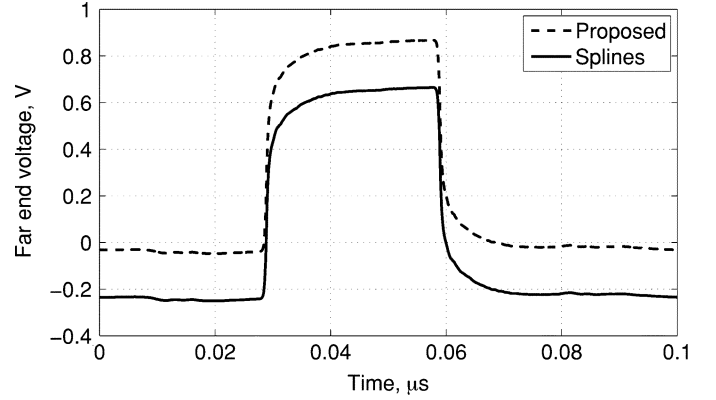


Fig. 17. Far end response of the interconnect link to a periodic digital signal, obtained with inverse FFT. Solid line was obtained from the raw dataset using standard spline interpolation. Dashed line was obtained using the proposed causality-constrained interpolation algorithm.

difference is due to the interconnect length, that makes the samples spacing (10 MHz) quite coarse. Since a real measurement of the dc point was not available to validate the reconstruction accuracy, we devised the following alternative test. The differential link is connected to 50-$\Omega$ resistors on ports 2, 3, 4 and to a voltage source with 50-$\Omega$ internal impedance on port 1. The voltage source applies a pulse of unit amplitude, 30 ns wide, and with a 0.15 ns rise time. The voltage at the far end of the line is depicted in Fig. 17 and shows how the large difference between the two reconstructed dc points affects the accuracy of the simulation result. Since the input pulse has a lower voltage level of 0 V, the output voltage is expected to have a vanishing dc baseline. However, the dc point obtained with spline interpolation leads to a transient response which is downshifted by more than 0.2 V. If the dc point is instead recovered with the proposed causality-controlled scheme, a much more realistic result is achieved. This example clearly points out the dramatic impact that simplistic data processing algorithms may have on the reliability of CAD simulations.

## VII. CONCLUSION

We presented a numerical technique based on the generalized Hilbert transform, which allows a precise characterization of the causality for tabulated frequency responses. Rigorous estimates for the numerical errors due to both finite sampling frequency and finite bandwidth have been derived and used in order to guarantee accuracy control and numerical robustness. The proposed algorithms allow to verify both causality and passivity of tabulated frequency responses coming from direct measurements or numerical field simulations. Thus, the results of this paper enable a data qualification process that can be inserted in the CAD workflow, in order to accept or reject frequency data based on physical consistency criteria. It is argued that many typical modeling and simulation problems might disappear if the root cause (flawed, inconsistent, or missing data) is removed by a suitable data qualification process.

## APPENDIX

### A. Bandpass Data Case

We consider here the case of bandpass data (12), for which the frequency response is available in

$$\Omega = [-\omega_{\max}, -\omega_{\min}] \cup [\omega_{\min}, \omega_{\max}].$$

The proposed algorithms are valid also in this case, with the minor modifications reported in this Appendix. If $\mathbb{L}(x)$ of (21) is redefined as

$$\mathbb{L}(x) = \ln \left| \frac{(\omega_{\max} + x)(\omega_{\min} - x)}{(\omega_{\max} - x)(\omega_{\min} + x)} \right| \tag{50}$$

all formulas in Sections III-B and III-D remain valid except for the bound [25], which includes now an additional term accounting for the missing low-frequency data

$$\begin{aligned}
T_n(\omega) = \frac{M}{\pi} \sum_{q=1}^{n} (\bar{\omega}_q)^\alpha &\left( \prod_{\substack{p=1 \\ p \neq q}}^{n} \frac{|\omega - \bar{\omega}_p|}{\bar{\omega}_q - \bar{\omega}_p} \right) \\
\times &\left\{ \left| \ln \frac{\omega_{\max} - \bar{\omega}_q}{\omega_{\max} - \omega} \right| - (-1)^{\alpha+n} \left| \ln \frac{\omega_{\max} + \bar{\omega}_q}{\omega_{\max} + \omega} \right| \right. \\
&+ (-1)^{n^+} \operatorname{sign}(\omega - \bar{\omega}_q) \left[ \ln \left| \frac{(\omega_{\min} - \bar{\omega}_q)\omega}{(\omega_{\min} - \omega)\bar{\omega}_q} \right| \right. \\
&\left. \left. + (-1)^\alpha \ln \left| \frac{(\omega_{\min} + \omega)\bar{\omega}_q}{(\omega_{\min} + \bar{\omega}_q)\omega} \right| \right] \right\}
\end{aligned} \tag{51}$$

where $n^+$ is the number of positive subtractions points $\bar{\omega}_q > 0$. This expression can be derived following the same guidelines
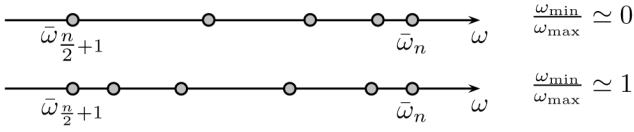
Fig. 18. Qualitative illustration of the optimal subtractions displacements for the limiting cases $\omega_{\min}/\omega_{\max} \simeq 0$ and $\omega_{\min}/\omega_{\max} \simeq 1$.

presented in Appendix B for the baseband case. A detailed proof is therefore omitted to avoid duplications.

We discuss now the displacement of subtraction points that should be adopted in the bandpass case in order to minimize the truncation error. For simplicity, we consider an even number of subtractions $n$, symmetrically placed around $\omega = 0$. Only the placement of the $n/2$ subtraction points $\bar{\omega}_{(n/2)+1}, \ldots, \omega_n$ laying in the positive frequencies axis is discussed, since the other $n/2$ points $\bar{\omega}_1, \ldots, \bar{\omega}_{n/2}$ can be easily obtained by symmetry with respect to $\omega = 0$. First, we place the two edge subtractions $\bar{\omega}_{(n/2)+1}$ and $\bar{\omega}_n$ close to $\omega_{\min}$ and $\omega_{\max}$, respectively, ($\epsilon \ll 1$)

$$\bar{\omega}_{\frac{n}{2}+1} = \omega_{\min} + (\omega_{\max} - \omega_{\min})\frac{\epsilon}{2} \tag{52}$$

$$\bar{\omega}_n = \omega_{\max} - (\omega_{\max} - \omega_{\min})\frac{\epsilon}{2}. \tag{53}$$

The position of the other subtraction points depends on the ratio $\omega_{\min}/\omega_{\max}$. We start by considering the two limiting cases $\omega_{\min}/\omega_{\max} \simeq 0$ and $\omega_{\min}/\omega_{\max} \simeq 1$. In the first case, since the available data cover the entire bandwidth $[-\omega_{\max}, \omega_{\max}]$ except for a very small interval $[-\omega_{\min}, \omega_{\min}]$, subtractions must be dense near $\omega = \omega_{\max}$ and rare at low frequency, where the missing bandwidth $[-\omega_{\min}, \omega_{\min}]$ is very small. A displacement similar to (26) is therefore optimal, provided that subtractions are not placed in $[-\omega_{\min}, \omega_{\min}]$. So we adopt the following rule

$$\bar{\omega}'_q = -(\bar{\omega}_n - \bar{\omega}_{\frac{n}{2}+1})\cos\left(\pi\frac{q-2}{n-2}\right) + \bar{\omega}_{\frac{n}{2}+1} \tag{54}$$

for $q = (n/2) + 1, \ldots, n$, which leads to a Chebyshev-like distribution of subtractions in $\Omega$. This distribution is depicted in Fig. 18 (top). In the second case, when $\omega_{\min}/\omega_{\max} \simeq 1$, subtractions must be concentrated near both $\omega = \omega_{\min}$ and $\omega = \omega_{\max}$. A Chebyshev distribution in the interval $[\omega_{\min}, \omega_{\max}]$ is therefore adopted

$$\bar{\omega}''_q = -\frac{\bar{\omega}_n - \bar{\omega}_{\frac{n}{2}+1}}{2}\cos\left(\pi\frac{q-\frac{n}{2}-1}{\frac{n}{2}-1}\right) + \frac{\bar{\omega}_{\frac{n}{2}+1} + \bar{\omega}_n}{2} \tag{55}$$

with $q = (n/2) + 1, \ldots, n$. This distribution is depicted in Fig. 18 (bottom). Based on the two displacements $\{\bar{\omega}'_q\}$ and $\{\bar{\omega}''_q\}$, a nearly-optimal grid for any value of $\omega_{\min}/\omega_{\max}$ can be obtained as a convex combination of the two

$$\bar{\omega}_q = \bar{\omega}'_q\left(1 - \frac{\omega_{\min}}{\bar{\omega}_{\max}}\right)^\gamma + \omega''_q\left(\frac{\omega_{\min}}{\omega_{\max}}\right)^\gamma. \tag{56}$$

We experimentally verified that (56) with $\gamma = 0.3$ approximately minimizes the truncation error bound (51) for any value
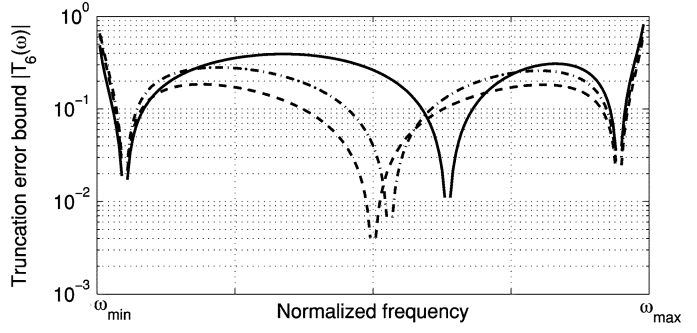


Fig. 19. Magnitude of the truncation error bound for $n = 6$ subtractions, for different $\omega_{\min}/\omega_{\max}$ ratios (solid line: $\omega_{\min}/\omega_{\max} = 0.01$, dashed–dotted line: $\omega_{\min}/\omega_{\max} = 0.5$, dashed line: $\omega_{\min}/\omega_{\max} = 0.99$).
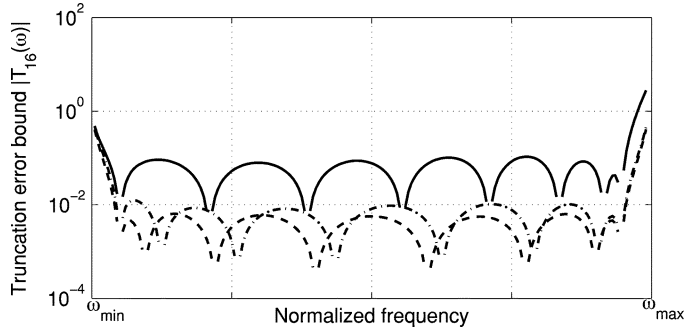


Fig. 20. As in Fig. 19 but for 16 subtraction points.

of $\omega_{\min}/\omega_{\max}$. Figs. 19 and 20 show how the proposed displacement rule approximately minimizes the truncation error bound for very different ratios of $\omega_{\min}/\omega_{\max}$, ranging from 0.01 to 0.99 and for different numbers of subtraction points ($n = 6$ and $n = 16$, respectively). We remark that this empirical rule, although being not optimal in mathematical sense, is sufficient for practical applications.

### B. Mathematical Proofs

We report here a detailed proof for the bound [25] on the truncation error (22) for the baseband case. Starting from (22) and taking the magnitude, we can write

$$|E_n(j\omega)| = \left|\frac{\prod_{q=1}^n(\omega - \bar{\omega}_q)}{j\pi}\int_{\Omega^C}\frac{-H(j\omega')}{\prod_{q=1}^n(\omega' - \bar{\omega}_q)}\frac{d\omega'}{\omega - \omega'}\right|$$

$$\leq \frac{\prod_{q=1}^n|\omega - \bar{\omega}_q|}{\pi}\underbrace{\int_{\Omega^C}\frac{|H(j\omega')|}{\prod_{q=1}^n|\omega' - \bar{\omega}_q|}\frac{d\omega'}{|\omega - \omega'|}}_{I_+ + I_-}.$$
$$\tag{57}$$

Let us denote with $I_-$ and $I_+$ the individual contributions to the integral in (57) due to the negative and positive frequencies, respectively

$$I_- = \int_{-\infty}^{-\omega_{\max}}\frac{|H(j\omega')|}{\prod_{q=1}^n|\omega' - \bar{\omega}_q|}\frac{d\omega'}{|\omega - \omega'|} \tag{58}$$

$$I_+ = \int_{\omega_{\max}}^{+\infty}\frac{|H(j\omega')|}{\prod_{q=1}^n|\omega' - \bar{\omega}_q|}\frac{d\omega'}{|\omega - \omega'|}. \tag{59}$$

Under the assumption (23), integrals (58) and (59) can be bounded with a closed form expression. For $I_+$, we have the following chain of inequalities

$$
\begin{aligned}
I_+ &= \int_{\omega_{\max}}^{+\infty} \frac{|H(j\omega')|}{\prod_{q=1}^{n} |\omega' - \bar{\omega}_q|} \frac{d\omega'}{|\omega - \omega'|} \\
&\leq M \int_{\omega_{\max}}^{+\infty} \frac{(\omega')^{\alpha}}{\prod_{q=1}^{n} (\omega' - \bar{\omega}_q)} \frac{d\omega'}{\omega' - \omega} \\
&= M \int_{\omega_{\max}}^{+\infty} \sum_{p=1}^{n} \frac{(\bar{\omega}_p)^{\alpha}}{\prod_{\substack{q=1 \\ q \neq p}}^{n} (\bar{\omega}_p - \bar{\omega}_q)} \frac{1}{\omega' - \bar{\omega}_p} \frac{d\omega'}{\omega' - \omega} \\
&= M \sum_{p=1}^{n} \frac{(\bar{\omega}_p)^{\alpha}}{\prod_{\substack{q=1 \\ q \neq p}}^{n} (\bar{\omega}_p - \bar{\omega}_q)} \frac{1}{\omega - \bar{\omega}_p} \ln \left| \frac{\omega_{\max} - \bar{\omega}_p}{\omega_{\max} - \omega} \right|.
\end{aligned}
\tag{60}
$$

The key step of this derivation is the partial fraction expansion of the second line. An analogous calculation shows that $I_-$ is bounded by

$$
I_- \leq M \sum_{p=1}^{n} \frac{(-\bar{\omega}_p)^{\alpha}}{\prod_{\substack{q=1 \\ q \neq p}}^{n} (\bar{\omega}_q - \bar{\omega}_p)} \frac{1}{\bar{\omega}_p - \omega} \ln \left| \frac{\omega_{\max} + \bar{\omega}_p}{\omega_{\max} + \omega} \right|.
\tag{61}
$$

A direct substitution of (60) and (61) into (57) leads to (25), concluding the proof.

This bound is the tightest possible for the considered class of functions, defined by (23). In fact, there exists a particular frequency response for which the magnitude of the truncation error (22) equals the bound (25). This response reads

$$
H(j\omega) = jM|\omega^{\alpha}|[\mathrm{sign}(\omega)]^{\alpha+n-1} \prod_{q=1}^{n} \frac{\omega - \bar{\omega}_q}{|\omega - \bar{\omega}_q|}
\tag{62}
$$

as can be verified by direct substitution. This proves that a tighter bounds does not exist, hence the proposed treatment of truncation errors is indeed optimal.

Finally, we remark that the above proofs are easily adapted to the bandpass case (12) with minor modifications, leading to the bound (51), which can be shown to be tight, as for the baseband case.

## ACKNOWLEDGMENT

## REFERENCES

[1] H. A. Kramers, "La diffusion de la lumiére par les atomes," in *Collected Scientific Papers*. Amsterdam, The Netherlands: North-Holland, 1956.

[2] R. Krönig, "On the theory of dispersion of x-rays," *J. Opt. Soc. Amer.*, vol. 12, pp. 547–557, 1926.

[3] K. R. Waters, J. Mobley, and J. G. Miller, "Causality-imposed (kramers krönig) relationships between attenusion and dispersion," *IEEE Trans. Ultrason. Ferroelecrt. Freq. Control*, vol. 52, no. 5, pp. 822–833, May 2005.

[4] S. Amari, M. Gimersky, and J. Bomemann, "Imaginary part of antenna's admittance from its real part using bode's integrals," *IEEE Trans. Antennas Propagat.*, vol. 43, no. 2, pp. 220–223, Feb. 1995.

[5] F. M. Tesche, "On the use of the hilbert transform for processing measured CW data," *IEEE Trans. Electromagn. Compat.*, vol. 34, no. 3, pp. 259–266, Aug. 1992.

[6] S. M. Narayana *et al.*, "Interpolation/extrapolation of frequency domain responses using the hilbert transform," *IEEE Trans. Microw. Theory Tech.*, vol. 44, no. 10, pp. 1621–1627, Oct. 1996.

[7] S. Luo and Z. Chen, "Iterative methods for extracting causal time-domain parameters," *IEEE Trans. Microw. Theory Tech.*, vol. 53, no. 3, pp. 969–976, Mar. 2005.

[8] R. Mandrekar and M. Swaminathan, "Casuality enforcement in translent simulation of passive networks through delay extraction," presented at the 9th IEEE Workshop Signal Propagation Interconnects, Garmisch-Partenkirchen, Germany, May 10–13, 2005.

[9] G. W. Milton, D. J. Eyre, and J. V. Mantese, "Finite frequency range Kramers-Krönig relations: Bounds on the dispersion," *Phys. Rev. Lett.*, vol. 79, pp. 3062–3065, 1997.

[10] K. F. Palmer, M. Z. Williams, and B. A. Budde, "Multiply subtractive Kramers-Krönig analysis of optical data," *Appl. Opt.*, vol. 37, no. 13, pp. 2660–2673, May 1998.

[11] V. Lucarini, J. J. Saarinen, and K. Peiponen, "Mutiply subtractive generalized kramers-krönig relations: Application on third-harmonic generation susceptibility on polysilane," *J. Chem. Phys.*, vol. 119, no. 21, pp. 11095–11098, Dec. 2003.

[12] A. Dienstfrey and L. Greengard, "Analytic continuation, singular-value expansions, and kramers-kronig analysis," *Inverse Probl.*, vol. 17, no. 5, pp. 1307–1320, Oct. 2001.

[13] M. R. Wohlers, *Lumped and Distributed Passive Networks*. New York: Academic, 1969.

[14] E. C. Titchmarsh, *Introduction to the Theory of Fourier Integrals*, 2nd ed. London, U.K.: Oxford Univ. Press, 1948.

[15] H. M. Nussenzveig, *Causality and Dispersion Relations*. New York: Academic, 1972.

[16] E. J. Beltrami and M. Wohlers, *Distributions and the Boundary Value of Analytic Functions*. New York: Academic, 1966.

[17] P. Triverio and S. Grivet-Talocia, "A robust causality verification tool for tabulated frequency data," presented at the 10th IEEE Workshop Signal Propagation Interconnects, Berlin, Germany, May 9–12, 2006.

[18] P. Triverio and S. Grivet-Talocia, "On checking causality of bandlimited sampled frequency responses," in *2nd Conf. Ph.D. Res. Microelectron. Electron. (PRIME)*, Otranto, Italy, Jun. 12-15, 2006, pp. 501–504.

[19] M. Abramowitz and I. A. Stegun, *Handbook of Mathematical Functions*. New York: Dover, 1968.

[20] W. Guttinger, "Generalized functions in elementary particle physics and passive system theory: Recent trends and problems," *SIAM J. Appl. Math.*, vol. 15, no. 4, pp. 964–1000, Jul. 1967.

[21] N. Ujević, "New error bounds for the simpsons quadrature rule and applications," *Comput. Math. Appl.*, no. 53, pp. 64–72, 2007.

[22] J. Mobley *et al.*, "Kramers-Krönig relations applied to finite bandwidth data from suspensions of encapsulated microbubbles," *J. Acoust. Soc. Amer.*, vol. 108, no. 5, pp. 2091–2106, Nov. 2000.

[23] P. Triverio, S. Grivet-Talocia, M. S. Nakhla, F. G. Canavero, and R. Achar, "Stability, causality and passivity in electrical interconnect models," *IEEE Trans. Adv. Packag.*, vol. 30, no. 4, pp. 795–808, Nov. 2007.

[24] B. Gustavsen and A. Semlyen, "Rational approximation of frequency domain responses by vector fitting," *IEEE Trans. Power Del.*, vol. 14, no. 3, pp. 1052–1061, Jul. 1999.

[25] R. Achar and M. Nakhla, "Simulation of high-speed interconnects," *Proc. IEEE*, vol. 89, no. 5, pp. 693–728, May 2001.

[26] P. Triverio and S. Grivet-Talocia, "Causality-constrained interpolation of tabulated frequency responses," in *IEEE 15th Topical Meeting Electr. Performance Electron. Packag.*, Scottsdale, AZ, Oct. 23–25, 2006, pp. 181–184.

**Piero Triverio** (S'06) received the Laurea Specialistica degree (M.Sc.) in electronics engineering, in 2005, from the Politechnic University of Turin, Turin, Italy, where he is currently working toward the Ph.D. degree in the Electromagnetic Compatibility Group. In 2005 and 2007 he was a visiting student with the Computer Aided Design Research Group at Carleton University, Ottawa, ON, Canada.

His research interests are in the modeling and simulation of high-speed interconnects.

Mr. Triverio is corecipient of the 2007 Best Paper Award of the IEEE TRANSACTIONS ON ADVANCED PACKAGING, and the recipient of the INTEL Best Student Paper Award presented at the IEEE 15th Topical Meeting on Electrical Performance of Electronic Packaging (EPEP 2006). He received the Optime Award of the Turin Industrial Association and in 2005 was selected for the IBM EMEA Top Student Recognition Event.

**Stefano Grivet-Talocia** (M'98–SM'07) received the Laurea and the Ph.D. degrees in electronic engineering from the Politechnic University of Turin, Turin, Italy.

From 1994 to 1996, he was with the NASA/Goddard Space Flight Center, Greenbelt, MD, where he worked on applications of fractal geometry and wavelet transform to the analysis and processing of geophysical time series. Currently, he is an Associate Professor of Circuit Theory with the Department of Electronics, the Polytechnic of Turin. His current research interests are in passive macromodeling of lumped and distributed interconnect structures, modeling and simulation of fields, circuits, and their interaction, wavelets, time-frequency transforms, and their applications. He is author of more than 90 journal and conference papers.

Dr. Grivet-Talocia served as Associate Editor for the IEEE TRANSACTIONS ON ELECTROMAGNETIC COMPATIBILITY from 1999 to 2001. He received the IBM Shared University Research (SUR) Award in 2007.